

Consolidating Lithiothermic-Ready Transition Metals for Li₂S-Based Cathodes

Zhenyu Xing, Guoqiang Tan, Yifei Yuan, Bao Wang, Lu Ma, Jing Xie, Zesheng Li, Tianpin Wu, Yang Ren, Reza Shahbazian-Yassar, Jun Lu,* Xiulei Ji,* and Zhongwei Chen*

Li₂S holds a promising role as a high-capacity Li-containing cathode, circumventing use of metallic lithium in constructing next-generation batteries to replace current Li-ion batteries. However, progress of Li₂S cathode has been plagued by its intrinsic drawbacks, including high activation potentials, poor rate performance, and rapid capacity fading during long cycling. Herein, a series of Li₂S/transition metal (TM) nanocomposites are synthesized via a lithiothermic reduction reaction, and it is realized that the presence of TMs in Li₂S matrix can transform electrochemical behaviors of Li₂S. On the one hand, the incorporation of W, Mo, or Ti greatly increases electronic and ionic conductivity of Li₂S composites and inhibits the polysulfide dissolution via the TM-S bond, effectively addressing the drawbacks of Li₂S cathodes. In particular, Li₂S/W and Li₂S/Mo exhibit the highest ionic conductivity of solid-phase Li-ion conductors ever-reported: 5.44×10^{-2} and 3.62×10^{-2} S m⁻¹, respectively. On the other hand, integrating Co, Mn, and Zn turns Li₂S into a prelithiation agent, forming metal sulfides rather than S₈ after the full charge. These interesting findings may shed light on the design of Li₂S-based cathode materials.

Li-ion batteries (LIBs) that operate on topotactic-intercalation reactions dominate the markets of portable electronics and electric vehicles (EVs).^[1] However, energy density of LIBs, albeit nearly reaching its ceiling, still cannot eliminate the drivingrange anxiety of EVs. For pursuing higher energy densities,

researchers have shifted their focus to battery systems based on conversion reactions.[2] Among candidate systems, the one having lithium sulfide (Li₂S) cathode coupled with silicon (Si) anode represents a highly promising battery system.^[3] On the Si anode side, conspicuous progress has been made toward securing high capacity and cycle cyclability.^[4] In contrast, the progress of Li₂S cathode has fallen behind, becoming a bottleneck for the Li₂S-Si battery system.

This stagnating situation arises from the processing difficulty of Li₂S-based composites and its intrinsic drawbacks as cathode materials. Specifically, preparation strategies for S₈-based composites are inapplicable to Li₂S-based composites due to Li₂S' high melting point, reactivity with humidity, and low solubility in most nonprotonic solvents. Moreover, Li₂S cathode suffers a high activation potential, poor rate capability, and rapid capacity fading.

First, the high activation potential forces a tradeoff between the capacity and cycle life. A high activation potential over 4 V is often indispensable to completely extract the Li-ions;^[5] however, a potential above 3.6 V will lead to decomposition of ether-based electrolytes, and consequent capacity fading. [6] Unfortunately,

Dr. Z. Xing, Prof. Z. Chen Department of Chemical Engineering Waterloo Institute for Nanotechnology Waterloo Institute for Sustainable Energy University of Waterloo Waterloo, Ontario N2L 3G1, Canada E-mail: zhwchen@uwaterloo.ca Dr. Z. Xing, Prof. X. Ji Department of Chemistry Oregon State University Corvallis, OR 97331, USA

E-mail: david.ji@oregonstate.edu Dr. G. Tan, Dr. Y. Yuan, Dr. J. Lu Chemical Sciences and Engineering Division

Argonne National Laboratory

Lemont, IL 60439, USA E-mail: junlu@anl.gov

The ORCID identification number(s) for the author(s) of this article can be found under https://doi.org/10.1002/adma.202002403.

Dr. Y. Yuan, Dr. R. Shahbazian-Yassar Department of Mechanical and Industrial Engineering University of Illinois at Chicago Chicago, IL 60607, USA Dr. B. Wang State Key Laboratory of Biochemical Engineering Institute of Process Engineering Chinese Academy of Sciences Beijing 100190, China Dr. L. Ma, Dr. T. Wu, Dr. Y. Ren X-Ray Science Division Argonne National Laboratory Argonne, IL 60439, USA Dr. J. Xie, Prof. Z. Li Key Laboratory of Cluster Science of Ministry of Education School of Chemistry and Chemical Engineering Beijing Institute of Technology Beijing 100081, China

DOI: 10.1002/adma.202002403

www.advancedsciencenews.com

www.advmat.de

when the upper cutoff potential is set to be 3.6 V, only less than a half of the theoretical capacity can be realized. Second, insulating nature of Li₂S causes large overpotentials and low energy efficiencies, especially at high current densities. Third, similar to the S_8 cathodes, the Li₂S cathode also suffers from the polysulfide (PS) dissolution and its resulting shuttling effect. [7]

To mitigate the activation potential, redox mediators, such as metallocenes, LiI, PS, and P₂S₅, have been investigated.^[8] These redox mediators are oxidized first during the anodic process and then in turn directly oxidize Li₂S on its particle surface, allowing the extension of the oxidation paths into the Li₂S particles' interior. Upon oxidizing Li₂S, the reduced redox mediators are regenerated. Repeating this process, Li₂S is activated throughout the remaining charge process of the first cycle. However, the redox mediator strategy has its own drawbacks. Of note, electrolyte-born redox mediators can oxidize the anode as well, forming undesirable solid electrolyte interphase (SEI) on the anode surface, which raises the anode's overpotential.^[9] With respect to the challenges of low conductivity and the PS dissolution, both Li₂S and S₈ have seen similar solutions.^[10] It has been suggested that transition metals (TMs) compounds can decrease the Li₂S activation potential by weakening the Li-S bonds or increasing the surface conductivity.[11] Regarding forming composites with Li₂S, TMs are known for the strong thiophilicity, which may render them as highly conductive PS adsorbents. [12] However, to date, it remains a challenge to form finely mixed composite materials of Li₂S with transition metals, where their distribution is uniform at the nanoscale.

Herein, we synthesized a suite of Li₂S/TM composites by a lithiothermic reduction reaction (LRR) and investigated the impacts of TMs on the Li₂S' electrochemical behavior. **Figure 1** schematically shows the fabrication of Li₂S/TM composites and their electrochemical reactivity. By reacting Li powder with a metal sulfide precursor, such as Ni₂S₃, FeS, CuS, CoS₂, MnS,

ZnS, MoS₂, WS₂, or TiS₂, Li₂S/TM composites are synthesized. Unfortunately, in the efforts to prepare composites of Li₂S/Ni, Li₂S/Fe, and Li₂S/Cu, agglomeration of Ni, Fe, and Cu occurs due to the crystal lattice mismatch between Li₂S and these three metals. However, in the cases of Li₂S/Co, Li₂S/Mn, Li₂S/Zn, Li₂S/Mo, Li₂S/W, and Li₂S/Ti, TM nanoparticles are distributed uniformly within Li₂S matrix. In spite of structural similarity, electrochemical behaviors of these Li₂S/TM nanocomposites were significantly different. Activation potentials of Li₂S/W, Li₂S/Mo, and Li₂S/Ti are lowered to 2.41, 2.57, and 3.65 V, compared to 3.78 V of the pure Li₂S. Moreover, rate capability and cyclability were dramatically improved when compared to pure Li₂S. At a current rate of 5C, capacities of Li₂S/W, Li₂S/Mo, and Li₂S/Ti can be maintained at about 440 mAh g⁻¹. As for long cycle evaluation, the incorporation of W, Mo, and Ti into the Li₂S matrix helps retain capacities at 582, 546, and 491 mAh g⁻¹ after 500 cycles, with very slow capacity fading rate of 0.068%, 0.077%, and 0.091% per cycle, respectively. Different from the Li₂S/W, Li₂S/Mo, and Li₂S/Ti, the introduction of Co, Mn, and Zn into Li₂S matrix renders the otherwise reversible Li₂S electrochemical pathways irreversible. More specifically, Li₂S/Co, Li₂S/Mn, and Li₂S/Zn are oxidized into corresponding metal sulfides as the final product rather than elemental sulfur after the charge process. As a result, Li₂S/Co, Li₂S/Mn, and Li₂S/Zn can only serve as prelithiation agents rather than active materials.

We propose the following LRR of transition metal sulfides (Ni_2S_3 , FeS, CuS, CoS₂, MnS, ZnS, MoS₂, WS₂, and TiS₂) to prepare Li₂S/TM nanocomposites.^[13] Herein, taking the Li₂S/Mo as an example

$$4Li(s) + MoS2(s) \rightarrow 2Li2S(s) + Mo(s)$$
 (1)

A mixture of Li/MoS₂ at the stoichiometric ratio is heated in a stainless steel tube under 650 °C for 5 h. To predict whether



Figure 1. Schematic of $\text{Li}_2\text{S}/\text{TMs}$ synthesis and proposed electrochemical reaction mechanism. Among these composites: I) $\text{Li}_2\text{S}/\text{Fe}$, and $\text{Li}_2\text{S}/\text{Cu}$ show megascopic metal agglomeration; II) $\text{Li}_2\text{S}/\text{Co}$, $\text{Li}_2\text{S}/\text{Mn}$, and $\text{Li}_2\text{S}/\text{Zn}$ show the irreversible Li_2S electrochemical behavior with an aptitude to be used as prelithiation agents; III) $\text{Li}_2\text{S}/\text{Mo}$, $\text{Li}_2\text{S}/\text{M}$, and $\text{Li}_2\text{S}/\text{Ti}$ demonstrate the reversible Li_2S electrochemical behavior, with the lowered activation potential, improved rate capability, and promoted cycling performance.

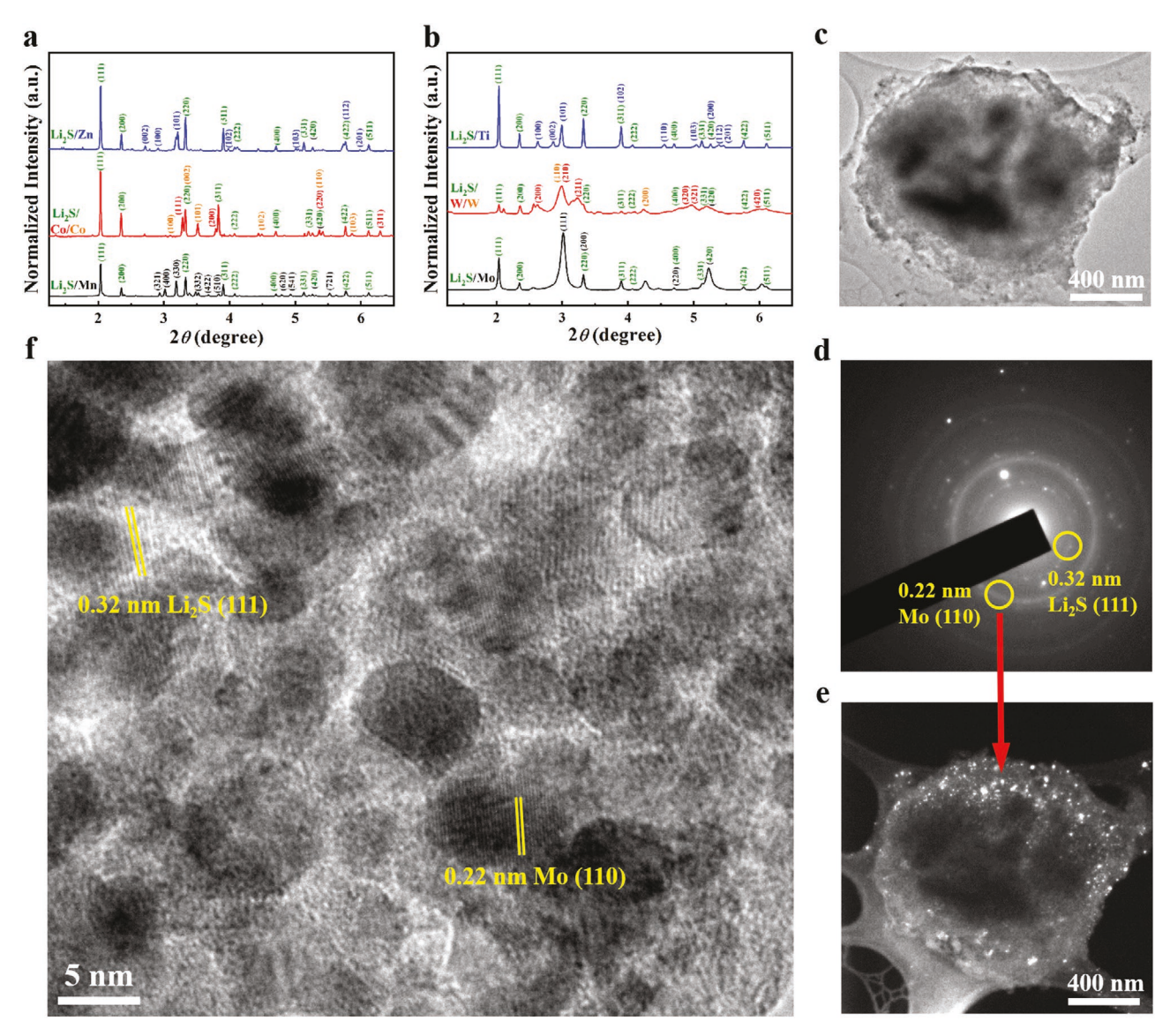


Figure 2. Structure and morphology and $\text{Li}_2\text{S}/\text{TM}$ nanocomposites. a) HEXRD patterns of the as-synthesized $\text{Li}_2\text{S}/\text{Cn}$, and $\text{Li$

the reaction is thermodynamically feasible, Gibbs free energy is calculated based on the following equation

$$\Delta G^{\circ} = \Delta H^{\circ} - T \Delta S^{\circ} \tag{2}$$

where G is the Gibbs free energy (kJ mol⁻¹), H is the enthalpy (kJ mol⁻¹), S is the entropy (kJ mol⁻¹ K⁻¹), and T is the temperature (K). Under isothermal and isobaric conditions, a negative ΔG value of -615.03 kJ mol⁻¹ indicates a highly spontaneous reaction. Thermodynamic calculations of other reactions show similar negative ΔG values, and the detailed calculations and results are summarized in Tables S1 and S2 in the Supporting Information.

A question is whether LRRs form intermediate ${\rm LiTM}_x{\rm S}_2$ phases via lithium intercalation in the layered compounds.

Both lab X-ray diffraction (XRD) patterns (Figure S1, Supporting Information) and synchrotron high energy X-ray diffraction (HEXRD) patterns (Figure 2) confirmed the absence of LiTM_xS₂ phases. Moreover, the peaks of metals and cubic Li₂S with a space group *Fm-3m* are identified as well. The LRR results in nanocomposites of Li₂S/Co, Li₂S/Mn, Li₂S/Zn, Li₂S/Mo, Li₂S/W, and Li₂S/Ti, whereas Ni, Fe, and Cu agglomerated into megascopic metal chunk (Figure S2, Supporting Information).

In this study, we will focus on $\text{Li}_2\text{S/Co}$, $\text{Li}_2\text{S/Mn}$, $\text{Li}_2\text{S/Zn}$, $\text{Li}_2\text{S/Mo}$, $\text{Li}_2\text{S/W}$, and $\text{Li}_2\text{S/Ti}$ nanocomposites with a molar ratio of 2:1, 1:1, 1:1, 2:1, 2:1, and 2:1, respectively. Table S3 in the Supporting Information listed domain sizes of Li_2S along the (111) direction and corresponding metals across specific crystal planes based on Scherrer equation. Domain sizes of Li_2S formed with Mo or W are 16–20 nm, much smaller than

those of Li₂S with Ti, Zn, Mn, and Co, which are over 28 nm. Moreover, the domain sizes of Mo and W are 7–10 nm, also much smaller than those of Ti, Zn, Mn, and Co, which are over 20 nm. The difference of domain sizes may relate to melting points of metals, which are 2623, 3422, 1246, 1495, 419, and 1668 °C for Mo, W, Mn, Co, Zn, and Ti, respectively. Based on our previous studies, LRR releases enormous heat, which raises reaction temperatures to approach the melting temperatures of Ti, Zn, Mn, and Co.^[14] Thus, the freshly formed Ti, Zn, Mn, and Co particles agglomerate, resulting in enlarged crystallite sizes. In contrast, Mo and W crystallites are small due to their inherently high melting points.

The Li₂S/TM composites were further characterized by high resolution transmission electron microscopy (HRTEM). Taking the Li₂S/Mo as an example, the composite is composed of micrometer-sized particles (Figure 2c). Rings found in the selected area electron diffraction (SAED) pattern confirm the existence of Li₂S and Mo in the form of polycrystalline (Figure 2d). The rings with d-spacings of 0.22 and 0.32 nm are attributed to Mo (110) planes and Li₂S (111) planes, respectively. Dark-field TEM imaging further reveals the uniform distribution of Mo particles (the bright dots) embedded in the Li₂S matrix (Figure 2e). This uniform heterogeneous structure is further confirmed by HRTEM (Figure 2f), where the darker lattice fringes on a particle sized of ≈7 nm are indexed to Mo (110) planes, while those with a 0.32 nm d-spacing of the lighter areas are ascribed to Li₂S (111) planes. Above results attest that Mo nanoparticles are uniformly distributed in the Li₂S matrix. Compared with the Li₂S/Mo, the analogical composite structures of Li₂S/W and Li₂S/Ti are shown in Figures S3 and S4 in the Supporting Information.

We investigated the electrochemical behaviors of Li₂S/TM composites. Galvanostatic charge/discharge (GCD) tests were performed at a current rate of 0.1C (1C = 1165 mAh g^{-1}). Li₂S/W, Li₂S/Mo, and Li₂S/Ti exhibit typical reversible Li₂S potential profiles (Figure 3a) whereas Li₂S/Mn, Li₂S/Co, and Li₂S/Zn present distinct irreversible electrochemical behaviors, which will be discussed later on (Figure 7a-c). Under a closer inspection of Figure 3a, the activation potential of Li₂S in GCD profiles has dropped from 3.78 V for pure Li₂S to 3.65, 2.57, and 2.41 V for Li₂S/W, Li₂S/Mo, and Li₂S/Ti, respectively, which is further confirmed by the lowered anodic onset potential in the cyclic voltammetry (CV) curves (Figure 3b) and decreased semicircle radius in the Nyquist plots (Figure S5, Supporting Information). Li₂S/W, Li₂S/Mo, and Li₂S/Ti deliver capacities of over 1500 mAh g⁻¹ at the end of the initial charge, while pure Li₂S can only provide a charge capacity of 640 mAh g⁻¹. As shown in Figure 3b, CV peaks attributed to Li₂S oxidation are located at 2.59 V for Li₂S/W, 2.68 V for Li₂S/Mo, 3.41 V for Li₂S/Ti, and 3.99 V for pure Li₂S.

Furthermore, the difference in the polarization patterns is also confirmed by ex situ electrochemical impedance spectroscopy (EIS) characterization at different state of charge (SOC) of GCD in the first cycle. Based on an equivalent circuit in Figure S6 in the Supporting Information, as-obtained Nyquist plots of Li₂S/W, Li₂S/Mo, Li₂S/Ti, and Li₂S in Figure S7 in the Supporting Information were fitted with two deconvoluted semicircles in the middle frequency range representing the charge transfer resistance ($R_{\rm ct}$) and interface contact resistance ($R_{\rm ic}$).

As summarized in Figure 3c, the sum of $R_{\rm ct}$ and $R_{\rm ic}$ between stages 1 and 5 (Figure S8, Supporting Information) clearly confirms that the introduction of W, Mo, and Ti into the Li₂S matrix lowers the reaction resistance by almost one order of magnitude in the initial activation process. According to the prior GCD profiles, CV scans, and Nyquist plots, we can conclude that introduction of W, Mo, and Ti into the Li₂S matrix not only lowers the activation potential, but also improves subsequent electrochemical reaction kinetics in the initial charge process.

It is likely that different extent of activation energy relates to conductivity of charge carriers. We measured the electronic conductivity and ionic conductivity of Li₂S/W, Li₂S/Mo, Li₂S/Ti, and pure Li₂S. Based on the direct current polarization (DCP) test and EIS measurement in Figure S9 in the Supporting Information, the total conductivity, electronic conductivity, and ionic conductivity of Li₂S/W, Li₂S/Mo, Li₂S/Ti, and Li₂S were calculated and summarized in Tables S4-S6 in the Supporting Information, respectively. To be specific, Li₂S/W, Li₂S/Mo, Li₂S/Ti, and pure Li₂S show electronic conductivities of 0.548, $0.343, 1.97 \times 10^{-5}, \text{ and } 1.17 \times 10^{-7} \text{ S m}^{-1}, \text{ respectively. Moreover,}$ the ionic conductivity is calculated to be 5.44×10^{-2} S m⁻¹ for $\text{Li}_2\text{S/W}$ and $3.62 \times 10^{-2} \text{ S m}^{-1}$ for $\text{Li}_2\text{S/Mo}$. Such high ionic conductivities of Li₂S-based composites have never been reported before. It should be noted that ionic conductivity values for Li₂S/Ti and Li₂S were calculated to be nearly nil due to the range limit of equipment, but otherwise close to 1×10^{-8} S m⁻¹, as reported elsewhere. Based on above results, Li₂S/W possesses the largest electronic conductivity and ionic conductivity, followed by Li₂S/Mo and Li₂S/Ti, while Li₂S has the smallest conductivities. The electronic conductivity and ionic conductivity trends coincide with that of activation potentials. Notably, ionic conductivities of the four are at least one order smaller than their corresponding electronic counterparts. Thus, it can be concluded that ionic conductivity is the determining factor for the activation potential if considering simultaneous transfer of electrons and Li+.

To attain an in-depth understanding of how the presence of W, Mo, and Ti in the Li₂S matrix lowers the activation potential from chemical views, beyond the physical parameters of ionic conductivity, spectra of X-ray photoelectron spectroscopy (XPS) were collected to characterize the Li+ bonding. As shown in Figure 3d, all Li 1s peaks of Li₂S/W, Li₂S/Mo, and Li₂S/Ti redshift from the Li-S binding energy in Li₂S of 56.38 eV, which reflects the weakened Li-S bonding in these composites. Hence, the extraction of Li⁺ in these composites may be more viable than that of pure Li₂S. To further understand how Li-S bond is weakened, X-ray absorption spectroscopy (XAS) was conducted. Taking Li₂S/Mo as an example, Mo edge position blue-shifts in X-ray absorption near edge structure (XANES) spectrum compared with Mo foil, which indicates a certain extent of charge transfer to sulfide (Figure 3e). In addition to the contracted Mo-Mo distance of R-space from Fourier-transformed extended X-ray absorption fine structure spectrum in Figure 3f, the existence of Mo-S bond is confirmed. Therefore, introduction of Mo weakens the Li-S bond due to induction effect from TM-S bond, which subsequently facilitates Li⁺ extraction.

To provide molecular insights into catalytic properties of metal species in Li₂S/metal composites, we carried out

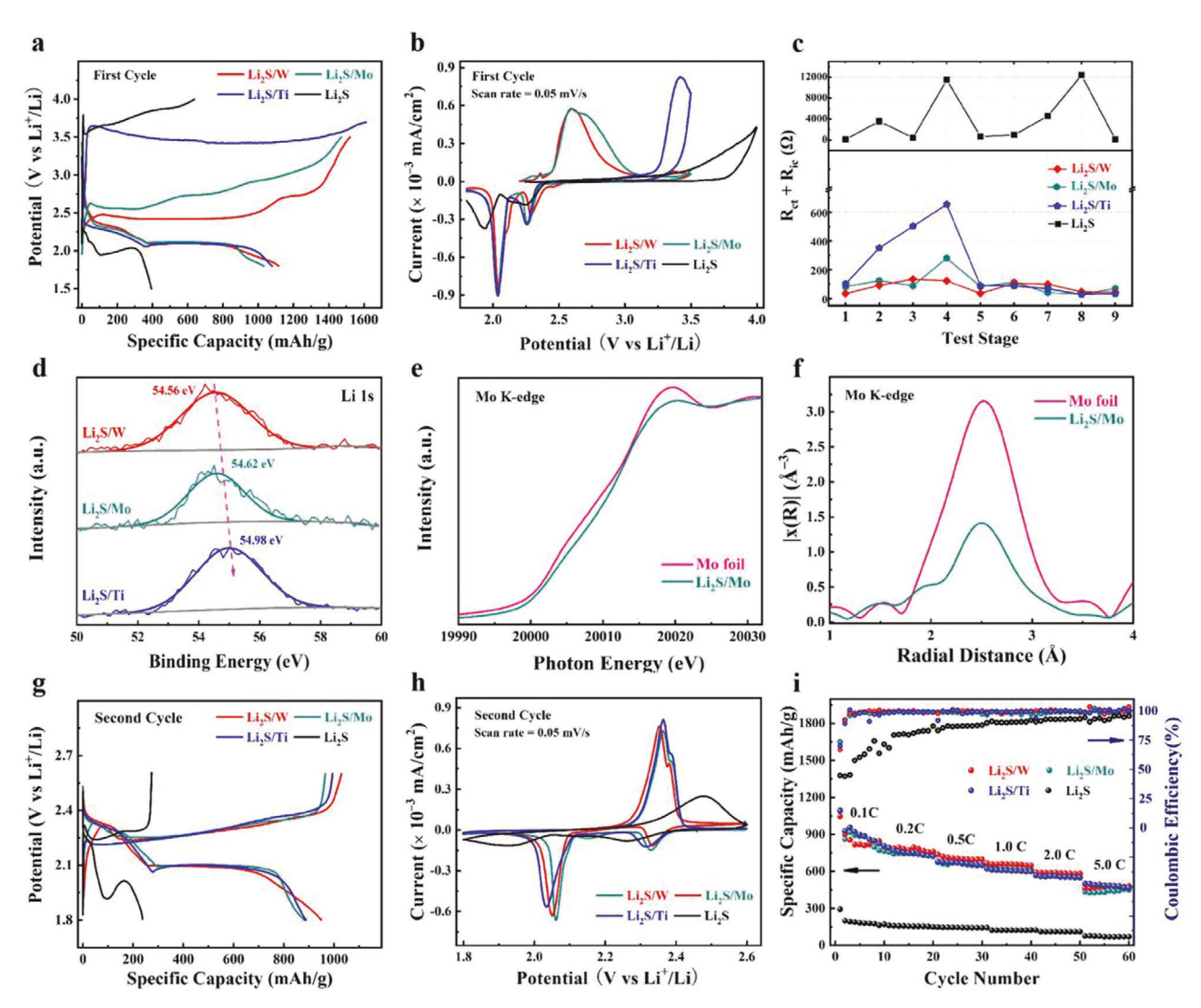


Figure 3. Electrochemical performance of Li_2S after the W, Mo, and Ti introduction. a) First GCD profiles of Li_2S/W , Li_2S/Mo , Li_2S/Ti , and pure Li_2S at a current density of 0.1C. b) First-cycle CV curves of Li_2S/W , Li_2S/Mo , Li_2S/Ti , and pure Li_2S at a scan rate of 0.05 mV s⁻¹. c) Sum of R_{ct} and R_{ic} for Li_2S/W , Li_2S/Mo , Li_2S/Ti , and pure Li_2S at different test stages of first cycle. d) XPS Li 1s spectra of Li_2S/W , Li_2S/Mo , Li_2S/Ti , and pure Li_2S . e) Mo K-edge XANES spectrum and f) Fourier-transformed Mo K-edge EXAFS spectrum of Li_2S/Mo and Mo foil. g) Second-cycle GCD profiles for Li_2S/W , Li_2S/Mo , Li_2S/Ti , and pure Li_2S at a current density of 0.1C. h) Second-cycle CV curves for Li_2S/W , Li_2S/Mo , Li_2S/Ti , and pure Li_2S at a scanning rate of 0.05 mV s⁻¹. i) Rate performance of Li_2S/W , Li_2S/Mo , Li_2S/Ti , and pure Li_2S at various current densities.

density functional theory (DFT) calculations. Based on the XRD (Figure 2b) and TEM results (Figures S2f, S3, and S4, Supporting Information), Mo (110), W (110), and Ti (101) surfaces were selected to represent the metal Mo, W, and Ti, respectively. As shown in Figure 4, we calculate Li₂S decomposition energy to evaluate delithiation reaction kinetics on the surface of these metals. Here, we consider that the initial charge process of Li₂S begins from an intact Li₂S molecule into a LiS cluster and a single Li⁺ (Li₂S \rightarrow LiS + Li⁺ + e⁻). The process involves Li⁺ moving away from Li₂S "molecules," accompanied by breaking of the Li-S bonds. As a result, reaction barriers on the Mo (110), W (110), and Ti (101) surfaces were calculated to be 0.91, 0.37, and 1.33 eV, respectively, agreeing well with the trend of activation potentials. Above DFT calculations corroborate how the TM-S bonds influence the Li+ extraction and resulted activation potentials.

Compared to the initial charge process, activation polarization disappears in subsequent cycles. As shown in Figure 3a, Li₂S/W, Li₂S/Mo, and Li₂S/Ti deliver discharge capacities around 1080 mAh g-1 with two plateaus located at 2.31 and 2.10 V, which is very similar to that when employing S_8 as the cathode material. However, pure Li₂S only delivers a discharge capacity of 400 mAh g⁻¹ and a much larger hysteresis of GCD profiles. As shown in Figure 3g, potential profiles of the second cycle show similar contrast of electrochemical properties between pure Li₂S, Li₂S/W, Li₂S/Mo, and Li₂S/Ti as those in the initial cycle. CV scans of Li₂S/W, Li₂S/Mo, and Li₂S/Ti in Figure 3b,h follow the same trend. Specifically, typical cathodic peaks located at 2.33 and 2.05 V shift upward while the anodic peaks at 2.36 V shift downward, as compared to pure Li₂S. The aforementioned difference of postactivation electrochemical behaviors between Li₂S/W, Li₂S/Mo, Li₂S/Ti, and pure Li₂S

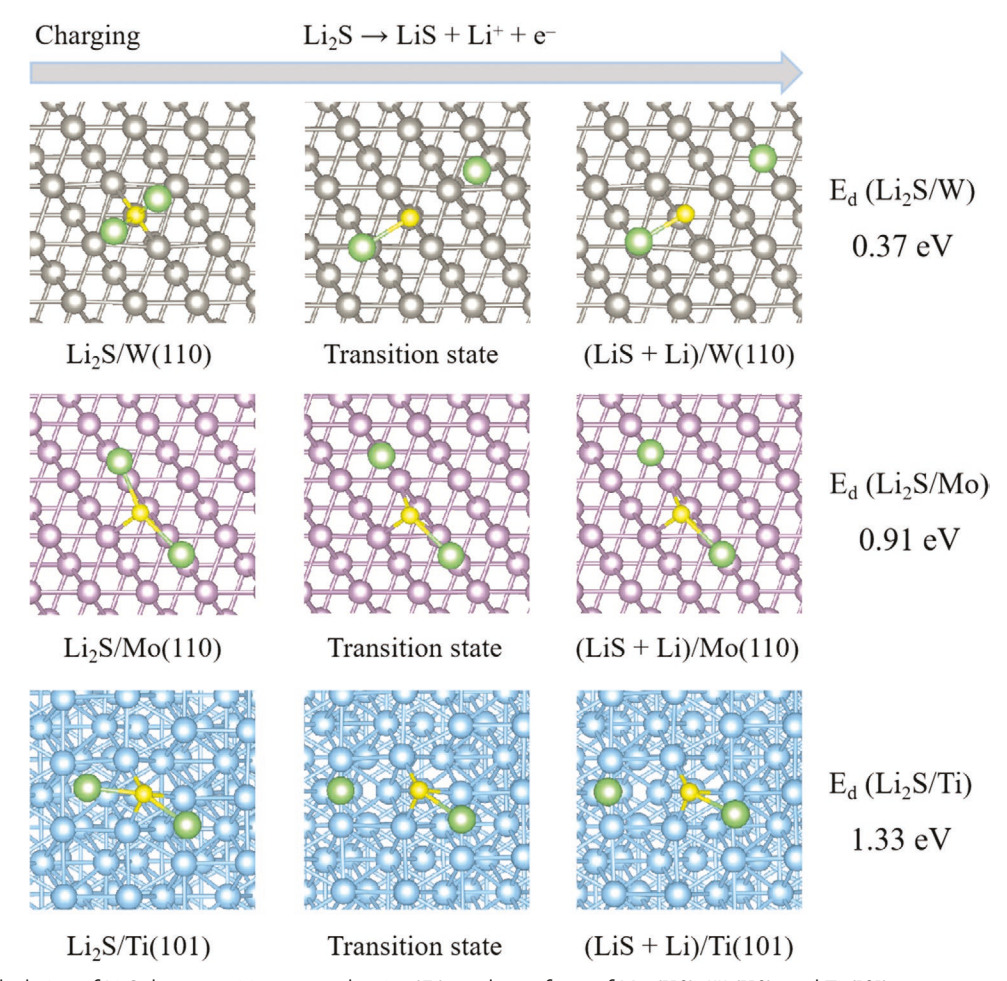


Figure 4. DFT calculation of Li_2S decomposition energy barrier (E_d) on the surfaces of Mo (110), W (110), and Ti (101).

indicates distinct electrochemical reaction kinetics, the reason of which results from two sources.

On the one hand, a fully activated Li2S, equipped with metal-sulfur bonds and weakened Li-S bonds, delivers much faster Li+ diffusion when compared with semiactivated and pure Li₂S. On the other hand, the introduction of W, Mo, and Ti into the Li_2S matrix also greatly facilitates electron transfer. The improved kinetics in the postactivation is further confirmed by ex situ EIS characterization. As shown in Figure 3c between stages 5 and 8, Li₂S/W, Li₂S/Mo, and Li₂S/Ti maintain an average reaction resistance of below 100 Ω , while the resistance of pure Li₂S greatly varies, even greater than two orders of magnitude. Moreover, this difference is further amplified when subjected to higher rate tests. Take Li₂S/Mo as an example; Li₂S/Mo delivers capacities of 914, 778, 689, 660, 585, and 440 mAh g⁻¹ under 0.1C, 0.2C, 0.5C, 1C, 2C, and 5C, respectively. In contrast, the capacities of pure Li₂S are only 178, 161, 143, 119, 113, and 65 mAh g^{-1} , under the same test conditions.

Aside from the activation potential and reaction kinetics, the long cycle tests were also conducted to evaluate the influence of introduction of Mo, W, and Ti at a current density of 0.5C. As shown in **Figure 5**a, the capacity of pure Li₂S drops from 332 to 150 mAh g⁻¹ after 140 cycles, at a capacity decay of 3.6% per cycle. In contrast, the capacity of Li₂S/W, Li₂S/Mo, and Li₂S/Ti was maintained at 582, 546, and 491 mAh g⁻¹ even after

500 cycles, respectively. The corresponding capacity fading rate is only 0.068%, 0.077%, and 0.091% per cycle, respectively. Evidently, the introduction of Mo, W, and Ti greatly improved the long-term cycle performance of $\rm Li_2S$.

Here, one possible reason for the improved cycle performance is that introduction of Mo, W, and Ti may alter the electrochemical pathway of Li₂S. More specifically, the formation of soluble Li-PS may be replaced by another intermediate, such as insoluble TM-PS. Thus, PS dissolution is circumvented and its resulting capacity fade is mitigated. However, this proposition is challenged by the GCD profiles and CV scans that exhibit the typical symptom of PS formation. To verify whether TM-PS forms, in situ time-lapse HEXRD is conducted to unravel the structural evolution. Taking Li₂S/Mo as an example, contour plots in Figure 5b for the initial cycle is collected and denoted by a red color for high intensity and a blue color for low intensity. During the charge process, the (111), (200), and (220) peaks indexed to be Li₂S, gradually weaken and eventually vanish. Concurrently, sulfur peaks begin to slowly emerge. In the subsequent discharge process, a reversible phase transformation between S and Li₂S occurs. Moreover, no other intermediate phase related to Mo is detected, which is also corroborated by the Mo (111) peak.

After discarding the possibility of TM-PS formation, the only rationale for the improved cycle performance is the

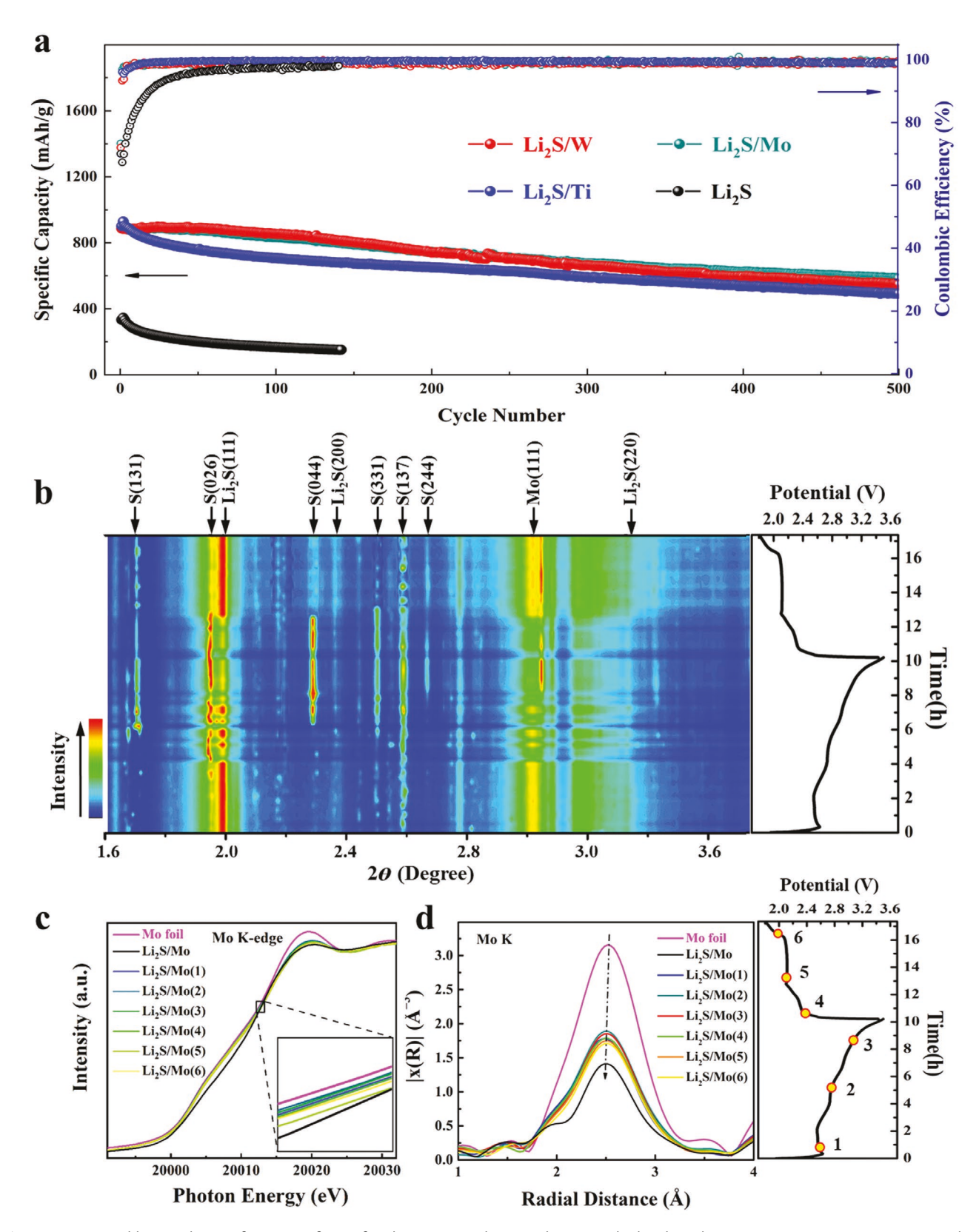


Figure 5. Improved long cycling performance of Li_2S after the W, Mo, and Ti introduction and related mechanism investigation. a) Long-term cycling performance of Li_2S/W , Li_2S/Mo , Li_2S/Mo , Li_2S/Ti , and pure Li_2S at a current density of 0.5C. b) In situ time-lapse HEXRD patterns of Li_2S/Mo electrode during the first charge–discharge process. c) Mo K-edge ex situ XANES spectrum and d) Fourier-transformed Mo K-edge EXAFS spectrum of Li_2S/Mo during the first charge–discharge process in contrast with metallic Mo.

controlled PS dissolution either via the physical confinement or chemical adsorption. According to HRTEM images, Li₂S/W, Li₂S/Mo, and Li₂S/Ti nanocomposites have TM nanoparticles embedded in the Li₂S matrix. Strictly speaking, there are no common physical boundaries for confinement of PS, as there are no porous structures or an outer shell to restrict PS dissolution. The rationale is the chemical bonding between TM and polysulfide, which has been demonstrated by Mo edge position blueshift from ex situ Mo K-edge XANES spectrum and contracted R-space Mo–Mo distance from Fourier-transformed EXAFS spectrum of Li₂S/Mo during the initial cycles (Figure 5c,d). Therefore, we considered that the Mo-S bond between Mo and PS during cycling aids to depress PS dissolution, and thus improve cyclability. Furthermore, DFT calculations were carried out to elucidate the binding strength between Li-PS (Li₂S_n, n = 3-6) species and TMs' surfaces. Taking the Li₂S/Mo as an example, Figure 6 depicts the molecular structures of Li-PS species and their binding structures onto the Mo (110) surface, with an average binding energy of 5.8 eV. This strong binding strength is well matched with the above XAS results, and it was considered to be attributed to the formation of Mo-S bond after S-S bond breaking of Li-PS. Intuitively, the side view of binding structures shows that two bottom S atoms are anchored to the Mo surface, providing a scaffold to support Li and other S atoms. More binding structures of Li-PS species onto the W (110) and Ti (101) surfaces are shown in Figures S10 and S11 in the Supporting Information, respectively. The calculated binding energies (Table S1, Supporting Information) indicate the strong binding between Li-PS species and three metal surfaces, suggesting their high capability in capturing Li-PS species to maintain good cyclability during charge/discharge processes.

In contrast with W/Li₂S, Mo/Li₂S, and Ti/Li₂S in Figure 3a, Co/Li₂S, Mn/Li₂S, and Zn/Li₂S showed irreversible electrochemical behaviors. As shown in **Figure 7**a–c, Co/Li₂S, Mn/Li₂S, and Zn/Li₂S deliver charge capacities of over 1000 mAh g⁻¹ up to their respective cut-off potentials. Similar to Ti/Li₂S and pure Li₂S, the charge potentials were all above 3 V. However, the discharge capacities of Co/Li₂S, Mn/Li₂S, and Zn/Li₂S in the following processes are negligible, where Co/Li₂S, Mn/ Li₂S, and Zn/Li₂S do not undergo typical S/Li₂S conversion reactions. To investigate the actual electrochemical process, electrode materials after the first charge process were collected and characterized by HEXRD. Based on the HEXRD patterns in Figure 7d-f, the final charge products are indexed to transition metal sulfides and unreacted Li2S/metals. Here, we speculate that Co, Mn, and Zn are electrochemically active in the charge process, which is quite different from the inertness found with W, Mo, and Ti. Subsequently, metal sulfides formed

Molecular structures of Li_2S_n (n =3-6)



Li₂S



 Li_2S_4

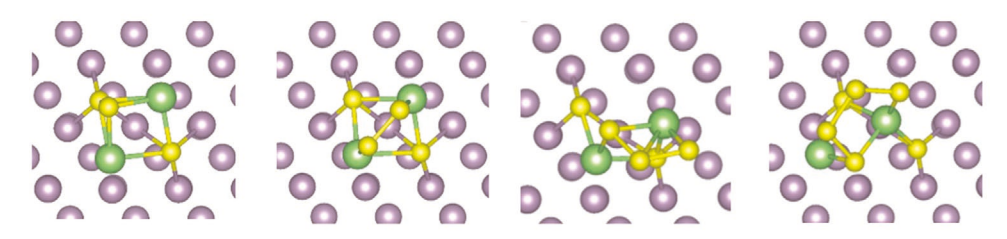


Li₂S₅



 Li_2S_6

$\text{Li}_2\text{S}_n/\text{Mo}(110)$ binding structures from top view



Li₂S_n/Mo(110) binding structures from side view

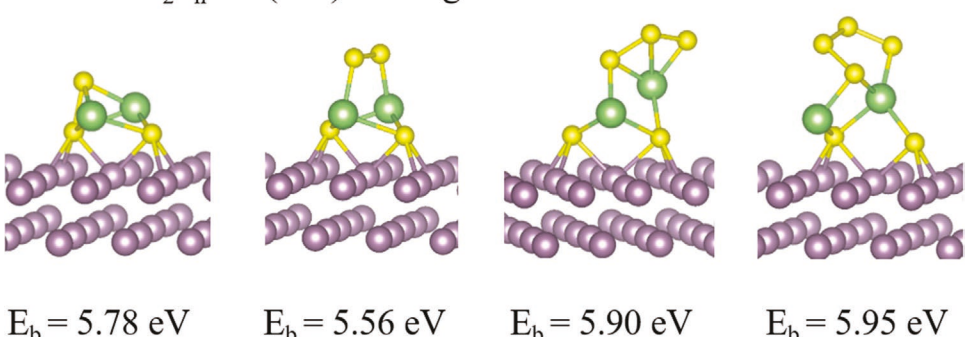


Figure 6. DFT calculations showing the binding structures of lithium polysulfide (Li_2Sn , n = 2-6) species onto the Mo (110) surface.

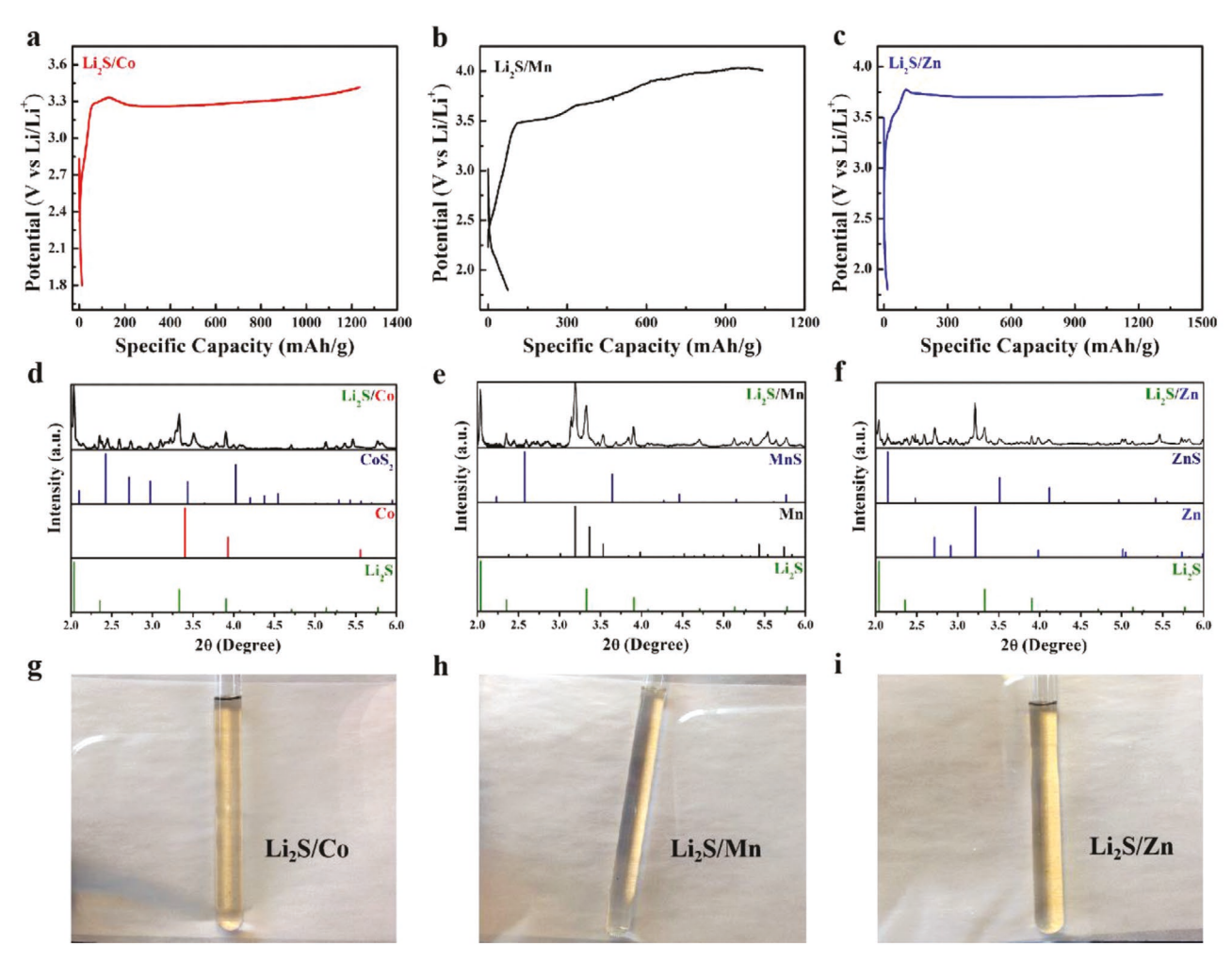


Figure 7. Irreversible electrochemical performance of Li_2S after introducing Co, Mn, or Zn. Galvanostatic charge/discharge profiles of a) Li_2S/Co , b) Li_2S/Mn , and c) Li_2S/Zn at a current rate of 0.1C in the first cycle. Ex situ HEXRD results of electrode materials of d) Li_2S/Co , e) Li_2S/Mn , and f) Li_2S/Co , after the first charge process. Digital photos of electrolytes from dissembled g) Li_2S/Co , h) Li_2S/Mn , and i) Li_2S/Cn cells.

by combining Co^{2+} , Mn^{2+} , and Zn^{2+} with S^{2-} . Beside the Co, Mn, and Zn, partial S^{2-} is also oxidized, forming PS shown in Figure 7g–i. Unfortunately, introducing Co, Mn, or Zn does not generate any benefits to the electrochemical performance of Li_2S as electrode materials. However, this result does not mean Co/Li_2S , Mn/Li_2S , or Zn/Li_2S is absolutely without merit. On the contrary, Co/Li_2S , Mn/Li_2S , or Zn/Li_2S can be used as a desirable cathode-prelithiation agent to compensate any loss of Li in a full cell. [15]

In summary, it is the first time that Li₂S/TM nanocomposites were synthesized by the lithiothermic reduction reaction, and the influence of TM on Li₂S electrochemical behavior was systematically studied. Li powder reacts with various metal sulfide precursors, where Ni, Fe, and Cu agglomerate into megascopic metal chunks in Li₂S/Ni, Li₂S/Fe, and Li₂S/Cu, while TMs were uniformly distributed into the Li₂S matrix of Li₂S/Co, Li₂S/Mn, Li₂S/Zn, Li₂S/Mo, Li₂S/W, and Li₂S/Ti. In spite of structural similarities, the electrochemical behaviors of these Li₂S/TM nanocomposites were different. The activation potentials of Li₂S/W, Li₂S/Mo, and Li₂S/Ti were dramatically lowered in contrast to pristine Li₂S due to the formed TM-S bond. Moreover,

the rate capability and cyclability have been dramatically improved also when compared with pure Li₂S. These improvements should be ascribed to the increased electronic/ionic conductivities and strong chemical adsorption between TMs and PS. Different from Li₂S/W, Li₂S/Mo, and Li₂S/Ti, introducing Co, Mn, and Zn into a Li₂S matrix renders the reversible Li₂S electrochemical pathway irreversible; that is, Li₂S will only oxidize into PS, rather than S, and the corresponding metal sulfide is found in the final product. As a result, Li₂S/Co, Li₂S/Mn, and Li₂S/Zn can act as the prelithiation agents rather than active electrode materials. Our findings are not only fundamentally distinguished, but also have a guiding significance in fabricating novel Li₂S-based cathode materials.

Experimental Section

Materials Synthesis: A mixture of Li and transition metal sulfides at the stoichiometric ratio was heated in a sealed stainless-steel tube with argon gas filled under 650 °C for 5 h via a one-step solid-state reaction. As-prepared samples were directly transferred to glovebox for future characterization and electrochemical test.

Materials Characterization: All the test samples were stored and fabricated in an argon-filled glovebox, and special precautions were taken during the material characterizations to prevent contamination from air. TEM and SAED measurements were carried out using a JEOL-3010 operated at 300 kV. Lab's XRD patterns were recorded using a MiniFlex 600 Rigaku Diffractometer with Cu K α irradiation ($\lambda=1.5406$ Å). HEXRD and XAS measurements were carried out at the 11-ID-C and 9-BM beamlines, respectively, Advanced Photon Source, Argonne National Laboratory. The samples were tightly sealed using the Kapton tape. HEXRD patterns were recorded in the transmission mode, and XANES and EXAFS spectra were recorded in the fluorescence mode.

Conductivity Test: The pressed pellets (10 mm in diameter) sandwiched between two gold foils were placed into the Swagelok for the EIS tests on Biologic VMP3 with a frequency range between 1 MHz and 1 Hz. For the DCP tests, the pellets were measured in the stainless-steel cell under 2 tons pressure.

Electronic partial conductivity and total conductivity were calculated based on the following equation

$$\rho = \frac{L}{R \times S} \tag{3}$$

Here, ρ is the conductivity, R is the resistance, S is the pellet area, and L is the pellet thickness.

It should be noted that the electronic resistance was calculated from the DCP tests followed by the equation

$$R = \frac{V}{I} \tag{4}$$

Here, *V* is the applied voltage and *I* is the measured current.

As for the ionic resistance, R was derived from the x-axis intercept from EIS tests as shown in Figure S9 in the Supporting Information. Ionic partial conductivity was calculated based on following equation

$$\frac{1}{\rho_i} = \frac{1}{\rho} - \frac{1}{\rho_e} \tag{5}$$

Here, $\rho_{\rm i}$ is the partial ionic conductivity, ρ is the total conductivity, and $\rho_{\rm e}$ is the partial electronic conductivity.

Electrochemical Test: Via a doctor-blade method, the slurry, consisting of 80 wt% Li₂S/TM or pure Li₂S, 10 wt% carbon black (Super-P), and 10 wt% poly(vinylpyrrolidone) (PVP), was coated on aluminum foil and dried at 80 °C in argon-filled glovebox. Coin cells were assembled with the as-prepared electrode as the working electrode, lithium metal as the counter/reference electrode, Celgard 2500 membrane as a separator, and 1 м lithium bis(trifluoromethanesulfonyl)imide (LiTFSI)/0.2 м LiNO₃ dissolved in 1,2-dimethoxyethane (DME) and 1,3-dioxolane (DOL) (1:1 by volume) as the electrolyte. The active mass loading was ≈2.0 mg cm⁻² with an electrolyte addition of 13 mL g_{sulfur}-1. The electrochemical measurements were performed on LAND battery cycler for galvanostatic charge-discharge test and Gamry 5000E workstation for CV test, where the voltage range was from 0.01 to 2.0 V versus Li+/Li. The specific capacities were normalized based on the sulfur mass. EIS results were obtained by Gamry 5000E workstation with the frequency range of 0.1 Hz to 100 kHz.

In Situ Synchrotron Measurements: In situ synchrotron HEXRD measurements during the cycling were carried out at the 11-ID-C beamline of the Advanced Photon Source, Argonne National Laboratory. A high-energy X-ray with beam size of 0.2 mm \times 0.2 mm and wavelength of 0.1174 Å was used to obtain 2D diffraction patterns in the transmission geometry. Homemade coin cells were charged/discharged at a constant current between 1.5 and 3.5 V using a MACCOR cycler. During the cell cycling, the XRD patterns were recorded using a Perkin-Elmer 2D X-ray detector placed at 1800 mm from the measured cells. The obtained 2D diffraction patterns were calibrated using a standard CeO2 sample and converted to 1D patterns of 2θ versus intensity using the Fit2D software.

Theoretical Calculations: All the DFT calculations were carried out using the GGA_PBE method with a plane wave basis set implemented in the Vienna Ab initio Simulation Package (VASP). The energy cutoff of 400 eV was used, and the Γ -point and a $2\times2\times1$ k-point mesh were used to sample the Brillouin zones for the surface systems. $5\times5\times4$ and $4\times4\times4$ supercells were used for Mo (110), W (110), and Ti (101) surfaces, respectively. All the atoms in the supercells were allowed to relax. The reaction barriers were calculated using climbing image nudged elastic band (CI-NEB) method.

Supporting Information

Supporting Information is available from the Wiley Online Library or from the author.

Acknowledgements

Z.C. acknowledges the financial support from the University of Waterloo, Natural Sciences and Engineering Research Council of Canada (NSERC), and the Waterloo Institute for Nanotechnology. X.J. acknowledges the financial support from the NSF No.1551693. Z.X. acknowledges the financial support with award Nos.18KJ04, 2018KQNCX059, 8S0478, and 2020A1515011549 and the schematic design by Serubbabel Sy. The work at Argonne National Laboratory was supported by the U. S. Department of Energy (DOE), Office of Energy Efficiency and Renewable Energy, Vehicle Technologies Office. Argonne National Laboratory is operated for DOE Office of Science by UChicago Argonne, LLC, under contract number DE-AC02-06CH11357. The use of the Advanced Photon Source beamline 9-BM and 11-ID-C, Office of Science user facilities, was supported by the U. S. DOE, Office of Science, Office of Basic Energy Sciences, under Contract No. DE-AC02-06CH11357. TEM measurements made use of instruments in the Electron Microscopy Service (Research Resources Center, UIC). R.S.-Y. acknowledges the financial support from NSF CBET-1805938. J.X. acknowledges the support from the Beijing Institute of Technology Teli Young Fellow Program (3100011181905).

Conflict of Interest

The authors declare no conflict of interest.

Author Contributions

Z.X., G.T., and Y.Y. contributed equally to this work. Z.X. conceived the concept and synthesized the materials; G.T. and Y.R. performed the in situ XRD experiments; Z.X. and B.W. conducted the electrochemical tests; L.M., G.T., and T.W. carried out the XAS experiments; Y.Y. and R.S.-Y. performed the TEM observation and data analyses; J.X. and Z.L. performed the DFT theoretical calculations; Z.X. and X.J. wrote the paper; Z.C., X.J., and J.L. supervised the project. All authors discussed the results and reviewed the manuscript.

Keywords

activation potential, Li-S bonds, lithiothermic reactions, lithium sulfide, transition metals

Received: April 7, 2020 Revised: May 15, 2020 Published online: June 25, 2020 www.advancedsciencenews.com



www.advmat.de

- [1] a) J. B. Goodenough, K.-S. Park, J. Am. Chem. Soc. 2013, 135, 1167;
 b) L. Lu, X. Han, J. Li, J. Hua, M. Ouyang, J. Power Sources 2013, 226, 272;
 c) Y. Yuan, J. Lu, Carbon Energy 2019, 1, 8.
- [2] P. G. Bruce, S. A. Freunberger, L. J. Hardwick, J.-M. Tarascon, Nat. Mater. 2012, 11, 19.
- [3] a) Y. Yang, M. T. McDowell, A. Jackson, J. J. Cha, S. S. Hong, Y. Cui, Nano Lett. 2010, 10, 1486; b) X. Liang, J. Yun, Y. Wang, H. Xiang, Y. Sun, Y. Feng, Y. Yu, Nanoscale 2019, 11, 19140; c) F. Wang, G. Chen, N. Zhang, X. Liu, R. Ma, Carbon Energy 2019, 1, 219; d) Z. Yan, H. Jin, J. Guo, Carbon Energy 2019, 1, 246.
- [4] a) C. K. Chan, H. Peng, G. Liu, K. McIlwrath, X. F. Zhang, R. A. Huggins, Y. Cui, Materials for Sustainable Energy: A Collection of Peer-Reviewed Research and Review Articles from Nature Publishing Group, World Scientific, Singapore 2011, pp. 187–191; b) M.-H. Park, M. G. Kim, J. Joo, K. Kim, J. Kim, S. Ahn, Y. Cui, J. Cho, Nano Lett. 2009, 9, 3844.
- [5] a) C. Zu, M. Klein, A. Manthiram, J. Phys. Chem. Lett. 2014, 5, 3986;
 b) Y. Yang, G. Zheng, S. Misra, J. Nelson, M. F. Toney, Y. Cui, J. Am. Chem. Soc. 2012, 134, 15387.
- [6] R. Miao, J. Yang, Z. Xu, J. Wang, Y. Nuli, L. Sun, Sci. Rep. 2016, 6, 21771.
- [7] a) Z. Xing, G. Li, S. Sy, Z. Chen, Nano Energy 2018, 54, 1;
 b) X. Ji, K. T. Lee, L. F. Nazar, Nat. Mater. 2009, 8, 500; c) Y. Yuan, G. Tan, J. Wen, J. Lu, L. Ma, C. Liu, X. Zuo, R. Shahbazian-Yassar, T. Wu, K. Amine, Adv. Funct. Mater. 2018, 28, 1706443; d) Y. X. Yin, S. Xin, Y. G. Guo, L. J. Wan, Angew. Chem., Int. Ed. 2013, 52, 13186; e) A. Manthiram, Y. Fu, Y.-S. Su, Acc. Chem. Res. 2013, 46, 1125.
- [8] a) F. Wu, J. T. Lee, N. Nitta, H. Kim, O. Borodin, G. Yushin, Adv. Mater. 2015, 27, 101; b) S. Meini, R. Elazari, A. Rosenman, A. Garsuch, D. Aurbach, J. Phys. Chem. Lett. 2014, 5, 915.
- [9] L. C. Gerber, P. D. Frischmann, F. Y. Fan, S. E. Doris, X. Qu, A. M. Scheuermann, K. Persson, Y.-M. Chiang, B. A. Helms, *Nano Lett.* 2016, 16, 549.

- [10] a) W. Xue, Z. Shi, L. Suo, C. Wang, Z. Wang, H. Wang, K. P. So, A. Maurano, D. Yu, Y. Chen, L. Qie, Z. Zhu, G. Xu, J. Kong, J. Li, Nat. Energy 2019, 4, 374; b) Z. W. Seh, J. H. Yu, W. Li, P.-C. Hsu, H. Wang, Y. Sun, H. Yao, Q. Zhang, Y. Cui, Nat. Commun. 2014, 5, 5017; c) Z. W. Seh, H. Wang, N. Liu, G. Zheng, W. Li, H. Yao, Y. Cui, Chem. Sci. 2014, 5, 1396; d) K. Cai, M.-K. Song, E. J. Cairns, Y. Zhang, Nano Lett. 2012, 12, 6474; e) Z. W. Seh, H. Wang, P.-C. Hsu, Q. Zhang, W. Li, G. Zheng, H. Yao, Y. Cui, Energy Environ. Sci. 2014, 7, 672; f) Y. Fu, Y. S. Su, A. Manthiram, Adv. Energy Mater. 2014, 4, 1300655.
- [11] a) M. J. Klein, A. Dolocan, C. Zu, A. Manthiram, Adv. Energy Mater.
 2017, 7, 1701122; b) G. Zhou, H. Tian, Y. Jin, X. Tao, B. Liu, R. Zhang, Z. W. Seh, D. Zhuo, Y. Liu, J. Sun, Proc. Natl. Acad. Sci. USA 2017, 114, 840; c) H. Yuan, X. Chen, G. Zhou, W. Zhang, J. Luo, H. Huang, Y. Gan, C. Liang, Y. Xia, J. Zhang, J. Wang, X. Tao, ACS Energy Lett.
 2017, 2, 1711; d) X. Fang, X. Guo, Y. Mao, C. Hua, L. Shen, Y. Hu, Z. Wang, F. Wu, L. Chen, Chem. Asian J. 2012, 7, 1013.
- [12] a) Y. Zhou, C. Wu, H. Zhang, X. Wu, Z. Fu, Electrochim. Acta 2007, 52, 3130; b) A. Hayashi, R. Ohtsubo, M. Tatsumisago, Solid State lonics 2008, 179, 1702; c) M. Obrovac, J. Dahn, Electrochem. Solid-State Lett. 2002, 5, A70.
- [13] a) G. Tan, R. Xu, Z. Xing, Y. Yuan, J. Lu, J. Wen, C. Liu, L. Ma, C. Zhan, Q. Liu, Nat. Energy 2017, 2, 17090; b) Z. Xing, J. Lu, X. Ji, Small Methods 2018, 2, 1800062; c) Z. Xing, N. Gao, Y. Qi, X. Ji, H. Liu, Carbon 2017, 115, 271; d) Z. Xing, X. Luo, Y. Qi, W. F. Stickle, K. Amine, J. Lu, X. Ji, ChemNanoMat 2016, 2, 692; e) Z. Xing, B. Wang, W. Gao, C. Pan, J. K. Halsted, E. S. Chong, J. Lu, X. Wang, W. Luo, C.-H. Chang, Y. Wen, S. Ma, K. Amine, X. Ji, Nano Energy 2015, 11, 600.
- [14] a) Z. Xing, B. Wang, J. K. Halsted, R. Subashchandrabose,
 W. F. Stickle, X. Ji, Chem. Commun. 2015, 51, 1969; b) Z. Xing,
 B. Wang, W. Gao, C. Pan, J. K. Halsted, E. S. Chong, J. Lu, X. Wang,
 W. Luo, C.-H. Chang, Nano Energy 2015, 11, 600.
- [15] Y. Sun, H. W. Lee, Z. W. Seh, G. Zheng, J. Sun, Y. Li, Y. Cui, Adv. Energy Mater. 2016, 6, 1600154.